

Fig. 20. Influence of the amount of dispersant on the rheological properties and curing behaviour. (a) Variation of the apparent viscosity of ceramic suspensions with the dispersant concentration at a shear rate of 46.5 s⁻¹ [146]. In-depth analysis of different amount of dispersant concentration in 80 wt% ceramic loaded ink [170]: (b) Rheological behaviour of ceramic suspensions with varying dispersant concentrations. The number (1, 2, 3) denotes the amount of dispersant in wt%. (c) Sedimentation properties of ceramic suspensions measured over different time periods. (d) Curing characteristics of ceramic suspensions, including conversion profiles and photopolymerization rates for different formulations under a reference light intensity. (e) SEM images showing the surface morphology of components produced at a light intensity of 3 mW/cm² and an energy dose of 30 mJ/cm². (f) Revised curing depth ($C_d - S_a$) as a function of energy dose. (g) Over-curing width of the cured suspensions with varying energy dose.

Reproduced from Ref.: (a) [146], and (b-g) [170], with permission from Elsevier.

curing depth. In contrast, a considerable amount of porosity prevails after the thermal treatment. This potentially decreases the piezoelectric characteristics of the sintered ceramic.

In this context, Hu *et al.* combined micro-stereolithography (μ SL) with the burnable plastic sphere (BURPS) technique to fabricate porous PZT ceramics [171]. Spherical PMMA particles with an average size of 20 μm were mixed in different weight fractions (5–35 wt%). The addition of the PMMA particles was found to increase the curing depth C_d (Fig. 22(a)). Similar variations of curing depths as a function PE content were also reported by Liu *et al.* (Fig. 22(b)) [172]. The authors also revealed that when the PE content was high (60 vol%), it can induce an inhomogeneous distribution of the PE particles due to increased viscosity. Therefore, an optimum concentration of these materials has to be used to have a balance between the density, porosity and piezoelectric properties.

Liu *et al.* studied the effect of incorporation of SS (20–50 vol%) to a ceramic suspension containing 40 vol% of PZT powders [150]. The authors reported that it was impossible to print without the use of the starch and that its addition significantly increased the curing depth and the printing accuracy. However, the inclusion of the starch granules led to an irregular and uneven surface finish due to the presence of larger particles. From the cross-sectional SEM image as shown in Fig. 22(c-f), the individual layers after printing can be easily identifiable when the starch content was at a volume fraction of just 20 %. With a subsequent increasing starch concentration, the inter-layer bonding increased. This

indicates the positive outcome of the addition of the starch, however at the cost of the density and functional properties (as discussed later in Section 3.2).

Liu *et al.* reported the effect of using various PS particles (3 μm , 8 μm , 16 μm) in a photocurable resin with PZT powder [173]. The curing depth was found to be in proportion to the polystyrene particle size. This is because of their relatively low RI and higher particle size compared to PZT ($d_{50} = 0.8 \mu\text{m}$). The surface morphology and the cross-section of the printed samples exhibited some noticeable features. The roughness increased with the particle size of the PS. The cross-section of the printed samples with PS particles of 16 μm exhibited delamination and cracks, probably due to inhomogeneous mixing (Fig. 22(h)). The sample produced using finer PS particles had a homogeneous distribution of the PS particles, with better inter-layer bonding (Fig. 22(g)). A similar conclusion was also reported elsewhere [145].

For ceramic suspensions containing both pore-forming agents and ceramic particles, the scattering behaviour should also be affected by the particle size and distribution of the ceramic particles (CPs) or PFAs (Pore Forming Agents) and difference in dimensions of the PFAs and CPs. In this regard, Kim *et al.* investigated the rheological and photocurable characteristics of a 70 wt% PZT ($d_{50} = 0.452 \mu\text{m}$) suspension containing 3.5 wt% of PMMA ($d_{50} = 5.86 \mu\text{m}$) [174]. Three ceramic suspensions were prepared by using distinct ball milling procedures, resulting in variations in the size of ceramic particles (fine, coarse, medium), as reported in Fig. 23(a). In general, the viscosity of a suspension increases

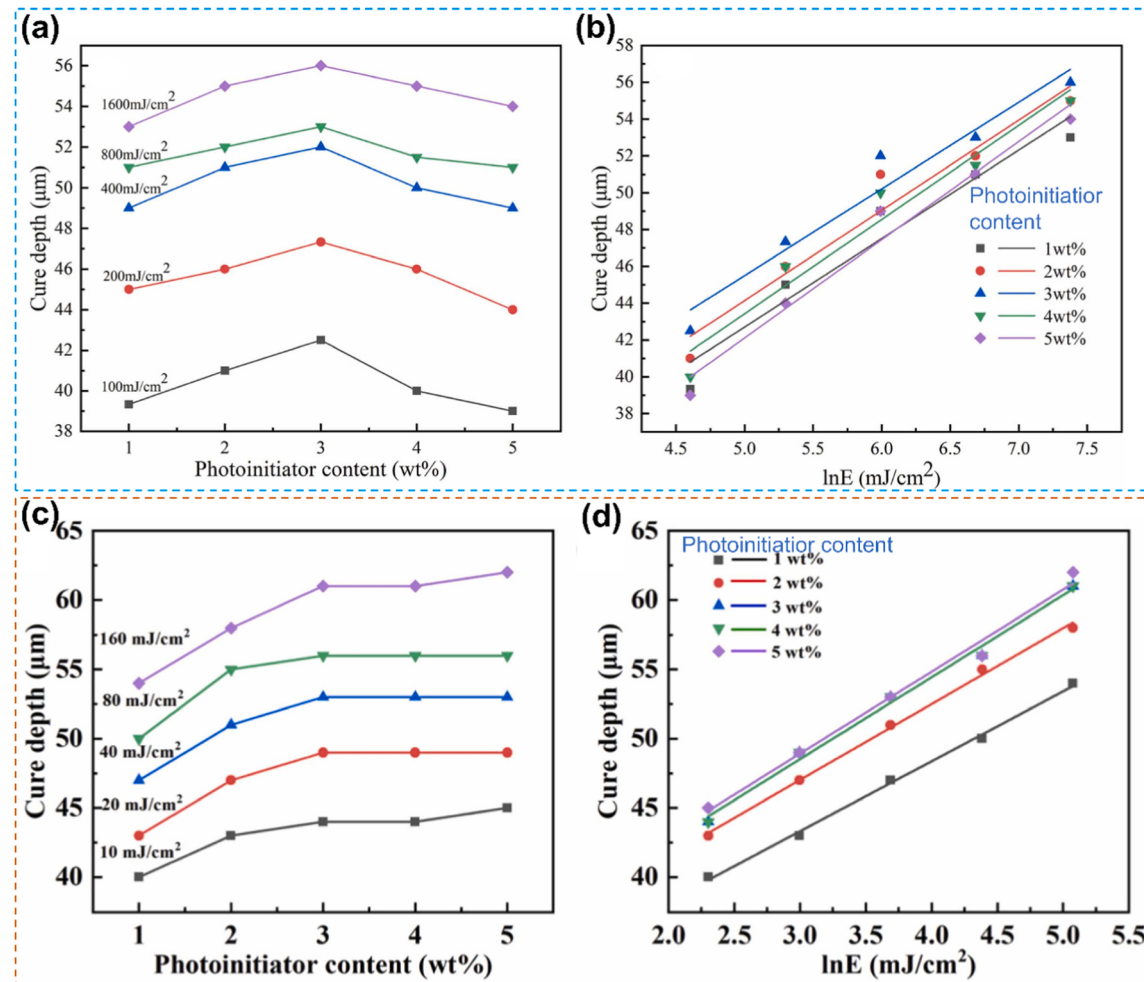


Fig. 21. Effect of the photo initiator concentration on the curing properties. Variation of the curing depth as a function of the (a, c) photo initiator content and (b, d) applied energy dose [148] [149].

Reproduced from Ref.: (a-b) [148], and (c-d) [149], with permission from Elsevier.

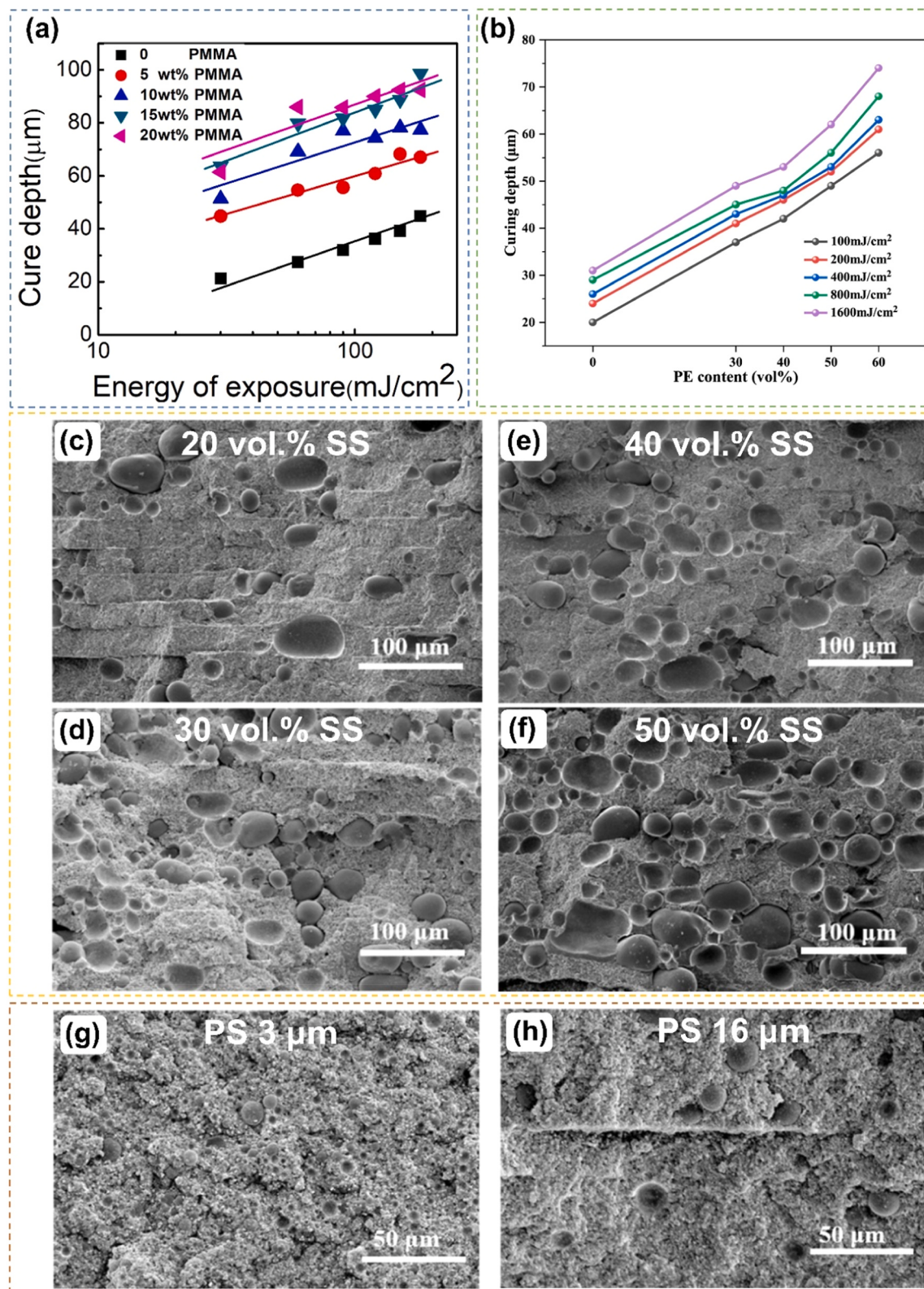


Fig. 22. Effect of the pore forming additives (PFAs) on the curing behaviour. (a) Curing depth as a function of energy dose with varying concentrations of PMMA (Polymethyl Methacrylate) [171]. (b) Curing depth variation as a function of PE content (Polyethylene) content and applied energy dose [172]. Cross-sectional SEM micrographs of PZT green parts with different (c-f) amount of soluble starch (SS) content [150], and (g-h) PS (polystyrene) particle size [173]. Reproduced from Ref.: (a) [171], (b) [172], (c-f) [150], and (g-h) [173], with permission from Elsevier.

with a decrease in the particle size. This is valid for a monomodal particle size distribution. In this case, the ceramic suspensions were bi-modal because of the size difference between the CPs and PFAs. Therefore, the suspension exhibited quite unusual viscosity dependence with the shear rate (Fig. 23(b)). The viscosity increased with an increasing ceramic particle size. In the case of fine CPs, the particles can easily fit into the voids generated by the packing of the PFAs and as a

result the liquid resin can escape easily from those voids resulting in an increased amount of mobile resin and enhancing the flow behaviour. As the size of the CPs increase, it can no longer get into the voids and the liquid resin is trapped in those voids. Hence, the viscosity increases as the size of the CPs approaches the size of the PFAs. The curing behaviours of the suspensions were in good agreement with the previously reported literature. C_d increases with increasing particle size, the energy

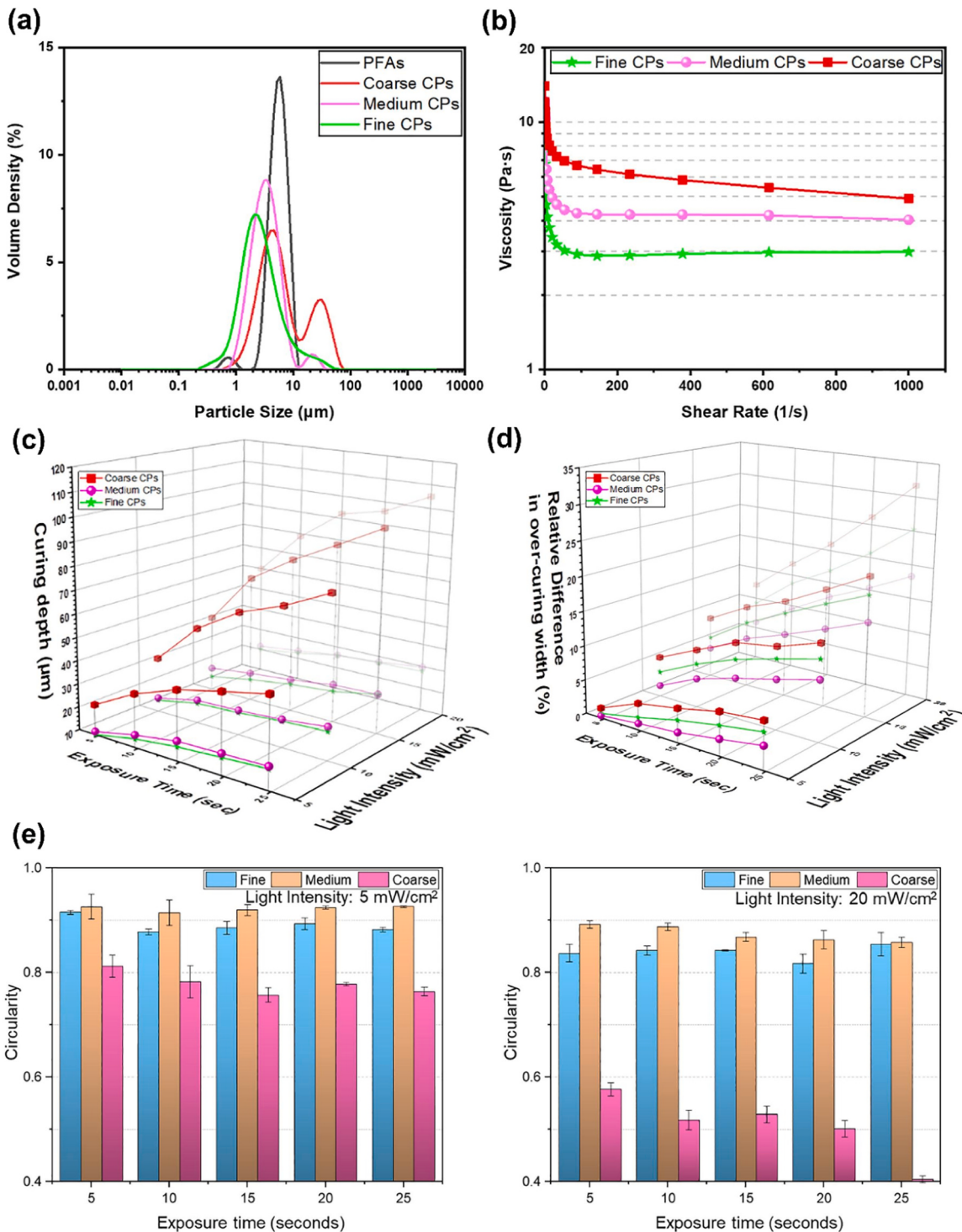


Fig. 23. Effect of the different ceramic particles (fine, coarse, and medium) in combination with PFAs leading to distinct particle size distributions and its impact on the rheological and curing ability [174]. (a) Particle size distribution for both ceramic particles (CPs) and pore-forming agents (PFAs), (b) Rheological properties of the suspension, (c) Curing depth (C_d) and (d) Over-curing width measurements, plotted against process parameters such as light intensity and exposure time, and (e) Analysis of circularity from laser confocal microscope images under different conditions of different light intensities.

Reproduced from Ref.: (a-e) [174], with permission from Elsevier.

dosage and the exposure time (Fig. 23(c)).

Furthermore, the scattering phenomenon induced by the ceramic particles is always reflected in the form of over-curing width. This was visualized by printing a circular pattern with all the ceramic suspensions at different intensities and exposure times. The suspension with the fine and medium sized ceramic particles exhibited uniform and isotropic solidification around the periphery. In contrast, the suspension with the coarse particles showed uneven and anisotropic solidification with irregular protrusions. These topological differences point to a difference in the light field distribution with particle size. Simulations performed by Qian *et al.* revealed that the over-curing width increases with the particle size [155]. However, in this study the observed trend was somewhat different and according to the following order: Coarse > Fine > Medium (Fig. 23(d)). For the fine and medium sized particles, the authors tried to correlate the observed trend for over-curing with the scattering efficiency \tilde{Q} (Eq. 12), however, no justification was found for the coarse particles. It was also reported that the over-curing width increased with increasing exposure time and energy. Further, circularity measurements were carried out to quantify the deviation. Suspensions with fine and coarse particles exhibited better circularity than the coarse ones (Fig. 23(e)). However, with increasing light intensity, the circularity values decreased. The surface roughness measurements revealed that the suspension with the coarse ceramic particles exhibited the roughest surface due to non-uniform packing density. Finally, it was reported that the interfacial properties between the PFAs and the CPs can be tailored easily by varying the particle size and the process parameters. The formation of a ceramic-polymer matrix with well-incorporated PFAs was achieved by using fine ceramic particles with a higher intensity of UV radiation. On the other hand, de-adhesion of PFAs from ceramic-polymer matrix and aggregation of the PFAs were observed for medium and coarse CPs respectively. The authors postulate that the reduced inter-particle distance between the fine CPs and PFAs makes the scattering process complicated, resulting in a strong adhesion force between the particles.

2.3.9. Novel ink formulations based on the sol-gel process

One of the most recent novel developments in feedstock formulation involves using the sol-gel technique to create UV-curable and particle-free compositions, as a possible alternative to traditional particle-based slurries. This means there are no particles suspended in the formulated system, which can reduce the scattering effects to a large extent and help in achieving a better resolution.

In this context, Rosental *et al.* developed a sol-gel formulation by employing the following steps [175]: an appropriate amount of barium acetate was dissolved in a solution composed of acetic acid and double-distilled water in a polyethylene terephthalate (PET) vial at 65 °C. Thereafter, this solution was cooled down to room temperature (RT) and poured in another PET vial containing appropriate amount of TTIP solution (TTIP + acetic acid) followed by vigorous stirring and sonication. After a few minutes, acrylic acid was added. In addition, acrylate monomer and the photo-initiator were introduced, followed by sonication. Sudan orange powder was used to control the penetration depth of the radiation. The authors also reported that the formulated ink exhibited no difference when printed using layer heights of 30 µm and 200 µm, with an exposure time set to 2 s. This is quite remarkable and is only possible because the ink contains no ceramic particles, thereby avoiding scattering. In contrast, inks containing piezoceramic particles typically require a longer exposure time, greater than 10 s, for layer thicknesses in the range of 10–50 µm (Table 4).

2.3.10. Steps to prepare the feedstock

The first step in the feedstock preparation process is the selection of the best monomer on the basis of the curing capacity and the viscosity. In situations when more than one monomer is being used, it is important to thoroughly combine them. Then the diluent, dispersant and photo-

initiator can be added to the prepared monomer system. One can also modify the as-received powders with a dispersant and then use it as a feedstock. The ceramic powder should be added in steps so that there is homogeneous mixing. After each step, the composite system has to be mixed well with the help of a planetary mill. To further homogenize and break the agglomerates, often a ball-milling step is employed. The duration and speed of the milling process depends on the nature of the agglomerates: hard or soft. After the addition of the photo-initiator, one needs to carefully handle the suspension: it should not be exposed to light. To avoid unwanted photo-chemical reactions, the photo-initiator can also be added after the ball milling step. In that case, the amount needs to be adjusted accordingly, as there is always some mass loss after the ball milling step during the feedstock transfer from the ball milling container to the vat.

2.4. Binder Jetting (BJ)

2.4.1. Basics of the technology

Binder jetting is an AM process in which a binder is selectively deposited using an inkjet print head on the powder-bed, in a layer-by-layer fashion. The green-part is taken out from the powder-bed and then de-powdered and is then cured, debinded and sintered to obtain the final product. The binder jetting process is well-known for its high volumetric output, thereby making it suitable for large scale productions. However, the need to use flowable coarse particles to generate the powder bed and the limited resolution of the technology (of the order of a few hundred microns) all contribute to a significant reduction in the density and the piezoelectric response of the printed parts decreases drastically.

The resolution of the printed components is dictated by the particle size, shape and size distribution. Despite the layer height ranging from 15 to 135 µm, as reported in Table 5, the resulting samples often exhibit low resolution due to factors such as binder spreading, limited powder packing density, and insufficient precision in the binder deposition process. A higher packing bed density is desired for high green and sintered density of the printed components. Binder selection and quantity (binder saturation) is another important parameter that greatly affects the printing process.

2.4.2. Particle shape, size and distribution

The properties that are mostly affected by the powder characteristics are the flowability, green density, powder-bed packing density and the sinterability as well as the residual porosity of the printed components. Bigger particles are often desired because of their increased flowability. In contrast, finer particles exhibit better sintering and functional properties. Spherical particles are preferred because they have fewer contact points and hence provide less resistance to flow, enabling the deposition of defect-free powder layers. In addition, a multi-modal particle size is often desired for better packing density as the smaller particles can fill in the void generated by the packing of the coarser particles.

Mariani *et al.* reported the Hausner ratio (H) of synthesized KNN powders to be 1.78 ± 0.1 , which was higher than the threshold value of 1.2 for powders with high flowability [191]. This higher value was correlated to the low density and irregular shape of the particles, along with the hygroscopic nature due to the presence of fine particles ($d_{50} = 310$ nm) and the formation of agglomerates due to high inter-particle-forces among the fine particles. In contrast, Sufiarov *et al.* synthesized spherical BCZT powders ($d_{10} = 10.3$ µm, $d_{50} = 31.8$ µm, $d_{90} = 100.4$ µm) by combining partial sintering of the initial powders followed by plasma spheroidization [192]. Hall funnel flowability index tests indicated a value of 50s/50g with an apparent density of 2.49 g/cm³. The relative density after sintering reached more than 90 % in this case. On the other hand, the relative density values were comparatively low (~40 – 60 %) when a non-optimized feedstock was used.

Several investigations have used commercial powders, which may be unimodal or poly-modal in size, with sphere-like or irregular

Table 5

Feedstock preparation and optimized printing parameters for binder jetting.

Feedstock	Particle size and morphology	Additives	Binder fluid	Binder saturation (%)	Printing parameters			Reference
					Feed to build ratio	Layer height (μm)	Miscellaneous	
BaTiO ₃	1 μm powder particles with agglomerates of 10 μm			60, 75, 100 and 120	2:1	15, 30	Binder cured at 195 °C	[196]
BaTiO ₃	$d_{50} < 3 \mu\text{m}$	PEMA	SOLUPOR, Hexane–1-ol, 2-ethylhexyl acetate, Hexyl acetate				Samples stored in drying cabinet 40 °C for 24 h	[197]
Hydroxyapatite	$d_{50} \sim 40 \mu\text{m}$ Spray-dried							
BaTiO ₃	0.85 – 1.45 μm			60, 75, 120	2:1	30		[195]
KNN	$d_{10} = 0.15 \mu\text{m}$, $d_{50} = 0.31 \mu\text{m}$, $d_{90} = 4.69 \mu\text{m}$	AquaFuse®		75, 90, 120		50	Powder bed cured at 180 °C for 6 h in air	[191]
BaTiO ₃	Micron multi-modal, $d_{10} = 0.1 \mu\text{m}$, $d_{50} = 3.4 \mu\text{m}$, $d_{90} = 25.4 \mu\text{m}$	CL001 cleaner	ExOne BS004	40 – 140 (steps of 20)		100	A lot of parameters has been disclosed, Cured at 180 °C for 3 h	[194]
	Submicron uni-modal, $d_{10} = 0.6 \mu\text{m}$, $d_{50} = 1.1 \mu\text{m}$, $d_{90} = 2.1 \mu\text{m}$			50 – 200 (steps of 50)		35		
BaTiO ₃	Non-spherical, $d_{10} = 0.67 \mu\text{m}$, $d_{50} = 2.04 \mu\text{m}$, $d_{90} = 4.30 \mu\text{m}$		AquaFuse® consisting of water, 10 – 30 % ethylene glycol, 10 – 30 % 2-butoxyethanol	175		15	Target bed temperature 40 °C, Cured at 200 °C for 10 h.	[198]
BCZT	Spherical, $d_{10} = 10.3 \mu\text{m}$, $d_{50} = 31.8 \mu\text{m}$, $d_{90} = 100.4 \mu\text{m}$			80		100		[192]
PZT-N	$d_{10} = 0.2 \mu\text{m}$, $d_{50} = 1.6 \mu\text{m}$, $d_{90} = 5.0 \mu\text{m}$		AquaFuse® consisting of water, 10 – 30 % ethylene glycol, 10 – 30 % 2-butoxyethanol	75, 90, 105		50	Curing at 180 °C for 6 h	[199]
BaTiO ₃	Max 45 μm		BS004 solvent, CL001 cleaner	100	1.75	135	Curing at 200 °C for 2 h	[200]

morphology, which is not an ideal scenario for creating a powder bed for the binder jetting process. In order to achieve spherical powders, additional experimental steps such as spray-drying are often required. However, these techniques may not be feasible for all researchers due to limitations in equipment or resources.

2.4.3. Binder saturation

The interaction between the binder and the ceramic powder is essential to achieve high accuracy printing and better green mechanical strength. The term binder saturation refers to the amount of binder dispensed as a function of powder-bed porosity. A value of 100 % binder saturation means all the empty voids have been filled by the binder.

Chavez *et al.* reported that with increasing the binder saturation content, the relative green density showed an upward trend [193]. This could be due to the incorporation of the binder in the powder bed pores and re-arrangement of particles with better packing density induced by the spreading action of the roller. However, an excessive amount of binder can limit the density of the green parts, as shown in Fig. 24. In another study, Sufiarov *et al.* optimized the binder saturation content by evaluating the deviation of the printed object from the CAD model [194]. It is important to note that at extremely low levels of binder saturation, green bodies are not strong enough to prevent delamination during either the curing, debinding and sintering processes. On the other hand, high saturation of the binder yields distorted parts.

2.4.4. Printing dynamics

The printing parameters determine the resolution of the printed parts to a great extent. Apart from the powder characteristics and binder saturation, the parameters that influence the printing accuracy are the layer height and the feed-to-build ratio.

The resolution in the z-direction is dictated by the layer height but is strongly dependent on the particle size of the initial feedstock. For instance, a layer thickness of 100 μm was chosen for a coarse barium titanate powder ($d_{10} = 0.1 \mu\text{m}$, $d_{50} = 3.4 \mu\text{m}$, $d_{90} = 25.4 \mu\text{m}$). Conversely, a layer height of 35 μm was chosen for the finer feedstock

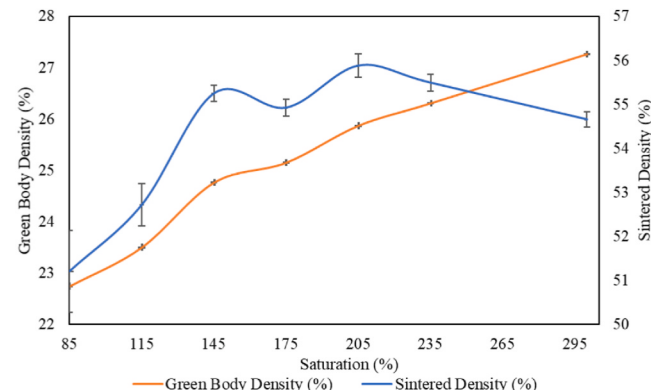


Fig. 24. Effect of binder saturation on the green body density and final sintered density of binder jet (BJ) printed BT ceramics [193]. [193], Open access article distributed under the terms of the Creative Commons CC BY license.

($d_{10} = 0.6 \mu\text{m}$, $d_{50} = 1.1 \mu\text{m}$, $d_{90} = 2.1 \mu\text{m}$) [194]. In general, for finer powders the minimum layer height should be at least thrice the diameter of the maximum particle size. This ratio can be decreased to one if the particles are spherical agglomerates. Nevertheless, the layer height obviously cannot be less than the particle size to avoid the formation of macroscopic defects when depositing the powders.

The feed-to-build ratio parameter controls the amount of powder transferred from the feeder to be utilized in the printing process. This helps in achieving a better powder packing ratio by depositing more powder on the printing site. Gaytan *et al.* reported a ratio of 2:1 [195]. This means that two layers of powder from the feed were used to fabricate one layer of the 3D printed object. Lowering this ratio was found to affect the surface finish of the powder bed.

There are several other parameters such as the roller speed, vibration frequency of the powder feeder, recoating speed, drying temperature,

drying time, etc. that can affect the process. However, as shown in Table 5, there is very limited literature available, and the effects of other unexplored parameters on the printing process have not yet been thoroughly investigated.

2.5. Selective laser sintering (SLS)

2.5.1. Basics of the technology

This process works similarly to the BJ technique. However, in this method, a high-powered laser is utilized to bond the ceramic particles, instead of a binder. The SLS process for processing ceramic components can be classified as: direct or indirect, depending on the starting feedstock [201]. If the initial feedstock has only ceramic particles, it is referred to as direct SLS. Conversely, if the ceramic powders are mixed with a polymer or binder with it, it is referred to as indirect SLS. In direct SLS, obtaining crack-free parts is challenging considering the poor resistance to thermal shock of ceramics. Furthermore, the short interaction time between the laser and ceramic powder limits the diffusion process, leading to a reduced density. In order to overcome these challenges, often binders are employed along with the powder, resulting in a polymer-ceramic composite after the printing process [202–204]. The presence of polymers or binders significantly reduces the required laser energy, as it is the polymer or binder that needs to be consolidated.

The technology is hardly suitable for use with ceramic powders, because of the high thermal gradients produced during 3D-printing, leading to defects or fractures in the sample. To mitigate thermal gradients that can cause internal stresses, leading to cracks or defects, a laser preheating or preheating at a certain temperature is often used before the SLS process [205,206]. In addition, the SLS equipment is expensive, using powerful infrared lasers. A strong advantage of this approach, however, lies in the possibility of obtaining already sintered parts that do not require a following high temperature heating step for consolidation. That means the processing parameters are directly linked to the sintered density of the ceramic, especially when the goal is to obtain pure ceramics, as is the case in this review paper.

The powder-bed requirements are similar to the ones of the binder jetting process. The most important parameters influencing the printing process include the powder size, laser power (W), scan speed (mm/s), beam diameter (μm or mm) and the powder feed ratio (g/min).

2.5.2. Process variables

The heating efficiency of the laser in irradiating the ceramic particles is strongly dependent on the absorption efficiency at the laser wavelength. In order to study the effect of particle size, Basile *et al.* studied the

effect of the single line scan on various powder fractions consisting of nano and micro powders by using a laser power of 22.8 W and scan speeds of 100, 500, 1000 and 1500 mm/s with laser energy densities respectively of 5.1, 1.0, 0.1 and 0.3 J/mm² [207]. The authors reported that with decrease in the scan speed, the laser energy density increases leading to an overall increase in width of the heat affected zone (Fig. 25 (a)). In addition, the width of the heat affected zone goes through a maximum on using a ratio of 70 % nanometric and 30 % micro powders for any given laser energy density. In any case, the addition of nanometric powders improves the heat absorbing capacity of the powder mix. The same authors reported the effect of the scan speed. A low scan speed (80 mm/s) lead to a highly dense microstructure with severe cracks (Fig. 25(b, d)). Conversely, with a higher scanning speed (600 mm/s) the severity of the cracks was suppressed however, the surface was characterized by a wave-like pattern (Fig. 25(c, e)). Nevertheless, such densification operates only in the top 5–10 μm .

Yu *et al.* reported that the scan speed needs to be adjusted accordingly to the laser power [208]. For instance, when the laser power was 9.7 W, the scan speed was varied from 22–65 mm/s. The moment the laser power was increased to 20.7 W, the scan speed was varied from 108–161 mm/s.

Gureev *et al.* reported the sintering depth varied with the laser power and the scanning speed [211]. At lower laser power, the sintered thickness was limited. However, with increasing power and decreasing speed, the sintered thickness increased which was accompanied by the laser-induced deformations (Fig. 25(f)). Since the laser power is directly related to the temperature generated, deviations from the optimized laser power can lead to defects. For instance, Zhang *et al.* reported that after the preheating procedure with a power of 2.5 W/mm² and a scanning rate of 60 mm/min, the surface of the sample was still completely flat [205]. However, on further increasing the power for the SLS process, the sample presented some defects in the form of V-shaped grooves, cracks, and melted powder agglomerates on the surface. The authors also reported that the densification was quite inhomogeneous: the top 500 μm exhibited dense layers >97 %, with the density decreasing to almost 76 % at a depth of 900 μm (Fig. 25(g)). Such improvement in the top 500 μm was related to the laser preheating step.

The density has been also reported to increase with the power and the irradiation time: increase in either of the factors leads to increase in the density. However, excessive power can also lead to the melting of nanometric BT powder [209]. In another study, the authors observed that increasing the power while decreasing the scan speed and powder feed rate resulted in higher laser energy input. This caused burning and evaporation of PZT, leading to non-uniformity in the printing process

Table 6
Feedstock preparation, optimized printing parameters, densification and functional properties for samples fabricated with selective laser sintering.

Feedstock	Particle size	Laser, Wavelength	Power _{max} (W)	Printing parameters			Density (%)	Additional information	Reference
				Power density / power	Scan speed (mm/s)	Beam diameter			
BaTiO ₃	50–70 nm	CO ₂ , 10.64 μm	40 W	3.5–3.7 W/mm ²	0.5	2.5 mm	98.7	Preheating: 2.5 W/mm ² with 60 mm/min, Difference in density in the top surface and bulk, $\epsilon_r = 200$ –1800	[205]
PZT		Nd:YAG	16 W	11–14.5 W	15–30	50 μm	1.65–2.00 g/cc		[211]
PZT		Nd:YAG	20 W	9.7–20.7 W	22–213	50 μm	2.1–4.1 g/sm ³		[208]
BaTiO ₃	$d_{50} = 0.44 \mu\text{m}$, $d_{50} = 50 \text{ nm}$	Nd:YVO ₄ , 1064 nm	22.8 W	Studied the effect of these parameters on the resulting samples				Coarse and fine powders used	[207]
PZT	1 μm	Nd:YAG	4 kW	150–300 W	5–15			Powder feed rate 1.3 g/min, $\epsilon_r = 430$, $\tan\delta < 5\%$	[210]
BaTiO ₃		CO ₂		5–8 W/mm ²		3.5 ± 0.5 mm	~92–98	Preheated upto 400 °C, Holding time during laser irradiation: 5–30 min	[209]
BiT		CO ₂		10–30 W		4 ± 0.5 mm	98	Preheated upto 350 °C, $(P_r) = 6.5 \mu\text{C}/\text{cm}^2$	[206]

[210]. Unfortunately, there have been very limited studies concerning SLS of piezoceramics, hence, the parameters affecting the printing process could not be addressed further.

3. Post-fabrication processing

The post-processing steps adopted for printed samples are determined by the specific AM processes used, whether they are classified as

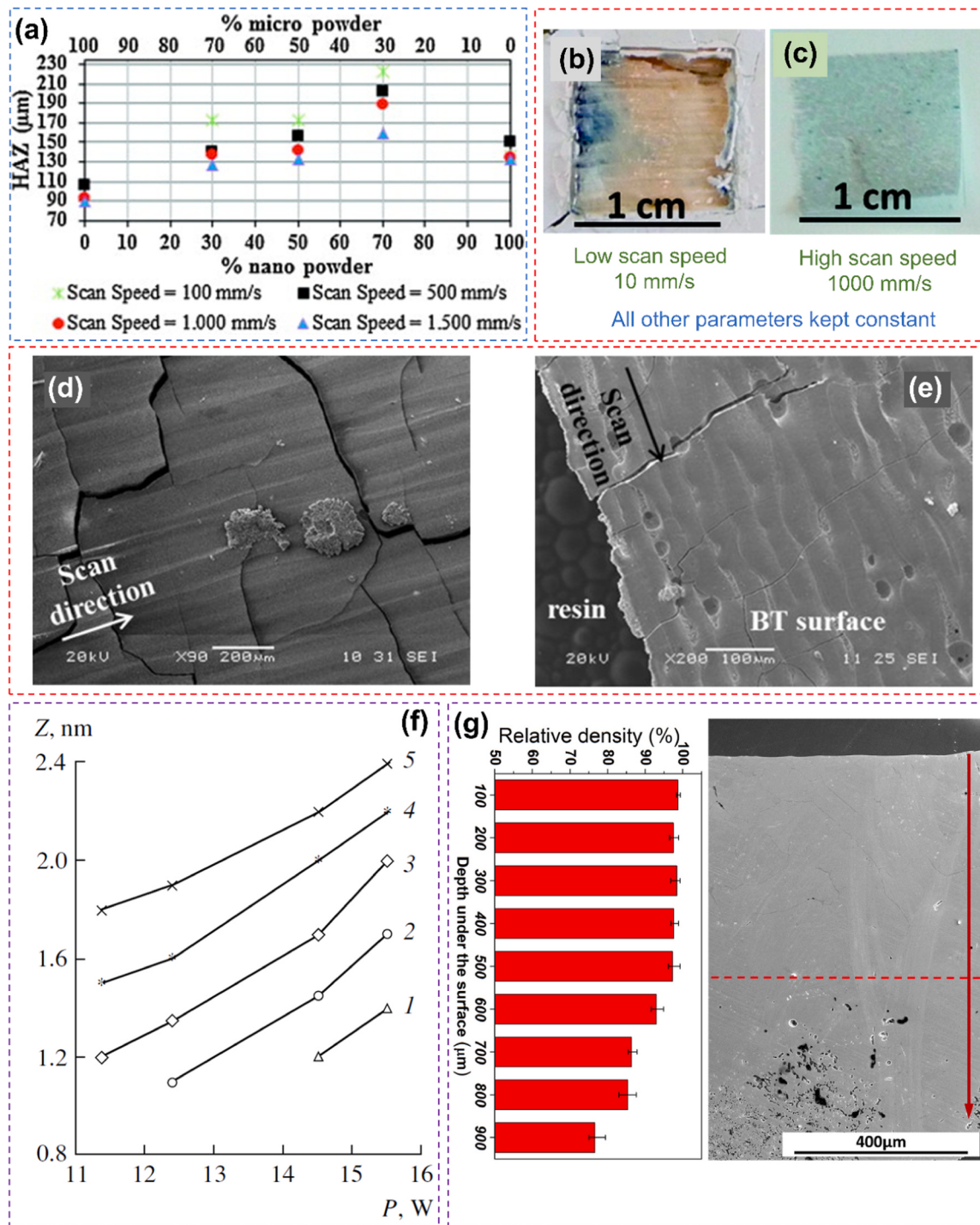


Fig. 25. Effect of the powder size, laser power and scan speed on the sintering depth and microstructure. (a) Variation of the heat affected zones (HAZ) as a function of the BT particle size and scan speed [207]. (b-c) Optical images, and (d-e) SEM images of BT samples sintered at different scanning speeds [207]. (f) Sintered layer thickness as a function of the laser power and scanning speed for PZT. The different speeds used are described as follows: (1) 60 mm/s (2) 30 mm/s (3) 20 mm/s (4) 15 mm/s (5) 12 mm/s [211]. (g) Inhomogeneity in the microstructure along the cross-section of the SLsed BT. The graph reveals the density variation with the depth from the surface [205].

Reproduced from Ref.: (a-e) [207], with permission from Elsevier. (f) [211], with permission from Springer Nature. (g) [205], with permission from John Wiley and Sons.

direct or indirect [33]. In direct AM methods, the material is selectively deposited only along the specified printing path to obtain the final form. Material extrusion-based techniques, such as DIW and FFF, fall under this category, hence no post-processing as such is required. However, DIW-fabricated samples are often subjected to controlled humidity conditions to guarantee uniform drying and to prevent any distortion or flaws that may arise during this process, particularly when the powder particles are fine and high solid loadings cannot be achieved.

In contrast, indirect AM methods often include the incorporation of the printed material inside a powder or resin bed, which must be subsequently cleaned or removed in order to obtain the finished product. This category of AM technologies includes VP, BJ and SLS. In VP, the printed green models are often cleaned in organic solvents (sometimes using ultra-sonic cleaning as well), such as alcohol or acetone, to remove uncured ceramic suspensions before drying at room temperature. Whereas, in BJ, the deposited binder is usually cured using heat to strengthen the green part before the de-powdering process.

Special care has to be taken for samples fabricated with novel feedstocks such as the ones mentioned in [Section 2.1.6](#) and [Section 2.3.9](#). For example, samples fabricated with capillary suspensions were printed on porous alumina plates (to remove some of the organic components by the action of capillary forces) and kept at ambient conditions for 5 days before thermal debinding [88]. Feedstocks based on sol-gel precursors are often subjected to an aging period before further processing [175].

3.1. Debinding

The main goal of the debinding procedure is to remove the binder used in the shaping process. The debinding process is heavily dependent on the type of binders that is used and can be classified into one of the following types: chemical (dissolving in a solvent), catalytic (using a catalytic acid vapour), wick (using capillary forces) or thermal (using a heat treatment) [212].

Chemical debinding is specifically employed when the binder system consists of a combination of two or more thermoplastic binders. One of the components, usually a low molecular weight polymer, is selectively dissolved in a solvent, that creates interconnected open porosity for the easy removal of the left-over binder during the thermal debinding process. The other components ensure that the green part is able to retain its shape during or after the debinding. This process is complex and requires careful attention since it involves the phenomena of dissolution and diffusion, which depends on the temperature, time and the powder characteristics. In a recent study, authors fabricated BT filaments with a blend of polyvinyl alcohol (PVA) and polycaprolactone (PCL) and partially removed the PCL by dissolving it in toluene at room temperature [113]. This partial removal of the binder helps in creating an interconnected open porosity, facilitating the subsequent binder removal during the thermal debinding step. Further, the removal of the PCL was confirmed by TGA and FTIR measurements. Poorly optimized chemical debinding processes, including solvent selection and parameters, may result in sample defects such as delamination or swelling. In contrast, catalytic debinding utilizes acid vapor to selectively remove one component of the binder system and is considered a faster debinding process compared to other methods.

The thermal debinding process is recognized as the most time-consuming and energy intensive in the entire fabrication procedure. Typically, slow heating rates are employed to ensure the complete removal of the binder and gradual, smooth decomposition of all organics. The heating rate during the thermal treatment process is found to affect the structural integrity of the printed structure and the densification process [143]. A rapid heating rate of 8 °C/min was reported to induce deformation and cracking in the printed structure, thereby leading to decreased density ([Fig. 26\(a-b\)](#)).

More recently, Kim *et al.* provided a detailed insight on the effect of the heating rate during the debinding step in order to preserve the porosity obtained after burning out of PMMA [189]. Three different

heating rates (0.5 °C/min, 1 °C/min, and 2 °C/min) were chosen in vacuum for debinding. The authors observed that the least shrinkage and highest density ([Fig. 26\(c-d\)](#)) was observed with a debinding rate of 1 °C/min and correlated with the decomposition behaviour of the organic matter in inert environment. The EDS analysis revealed that the sample debinded at 1 °C/min sample had the lowest carbon content, followed by 0.5 °C/min and 2 °C/min. This is because the heating rate during vacuum debinding affects how quickly the decomposition products move from inside the sample to the surface. At a lower heating rate (0.5 °C/min), the gas generated from the pyrolysis of the organic matter builds up inside because it cannot escape fast enough, but the longer heating time helps some carbon on the surface evaporate. In contrast, at a higher heating rate (2.0 °C/min), a film forms on the surface due to quick binder flow, but there is not enough time for carbon to evaporate, leading to more carbon residue. This conclusion was further supported by the roughness measurements, which showed a similar trend to the carbon content levels suggesting the roughness was affected by the residual carbon ([Fig. 26\(e\)](#)). Most importantly, the optimal debinding rate ensured that the pore size distribution matches well with the particle size distribution of the PMMA particles after sintering.

During the DIW process, the solvent (typically deionized water, as reported in [Table 2](#)) evaporates from the sample after printing, leaving behind a small amount of organics that can be thermally removed. Since the amount of organics remaining is minimal (similar to binder jetting), the thermal debinding process is relatively straightforward. This is also applicable for samples fabricated using binder jetting technology. Most of the studies have reported a debinding rate of 1–5 °C/min ([Table 8](#)), which is often accompanied with a certain dwell time at temperatures where complete decomposition of the binder or additives is anticipated. These temperatures are usually determined by performing TGA analysis on the prepared feedstock.

The debinding scenario is similar for the samples fabricated with VP technique. Thermoset polymers undergo irreversible cross-linking during the curing process, making them resistant to all methods of debinding except thermal treatment. As opposed to DIW, the monomer that serves as the solvent in this case does not evaporate. As a result, the process of thermal debinding is challenging and requires special attention while designing the debinding schedule. The thermal debinding process is slow and can last up to a few days with a debinding rate limited to a maximum of 1 °C/min ([Table 10](#)). It is important to keep in mind that researchers often prefer to carry out the thermal debinding process in an inert atmosphere, either argon (Ar), nitrogen (N₂) or vacuum ([Table 10](#)). The binder decomposition behaviour is strongly influenced by the debinding atmosphere [213]. Organic compounds undergo vigorous exothermic reactions due to oxidative decomposition in the presence of air, which may result in the formation of defects such as cracks or delamination ([Fig. 27\(a\)](#)). Such defects have been reported by several authors [159,165]. On the other hand, the exothermic behaviour is significantly inhibited in inert atmospheres due to the absence of oxygen and the decomposition proceeds through the disruption of the chemical bonds by heat absorption [214]. As a result, a certain amount of carbon remains in the sample leading to a black colour ([Fig. 27\(b\)](#)), which is subsequently eliminated by a second debinding process in the presence of air ([Fig. 27\(d\)](#)). Certain additives such as polyethylene (PE) swells when heated in argon, thus making the process complicated [172]. In such a scenario, debinding in argon is not recommended. The best way to design a debinding schedule is to perform a TGA analysis and using this data to plot the DTG (or DSC to observe the endothermic or exothermic peak) to see the peaks where the most intense mass loss occurs ([Fig. 27\(c\)](#)). To ensure the integrity of the printed structure during the binder removal process, it is important to employ a slow heating rate and/or dwell time in regions where strong decomposition occurs so as to facilitate gradual and smooth removal of organics. Sometimes, low-temperature volatile additives are employed to generate a network of transient porosity that facilitates the removal of

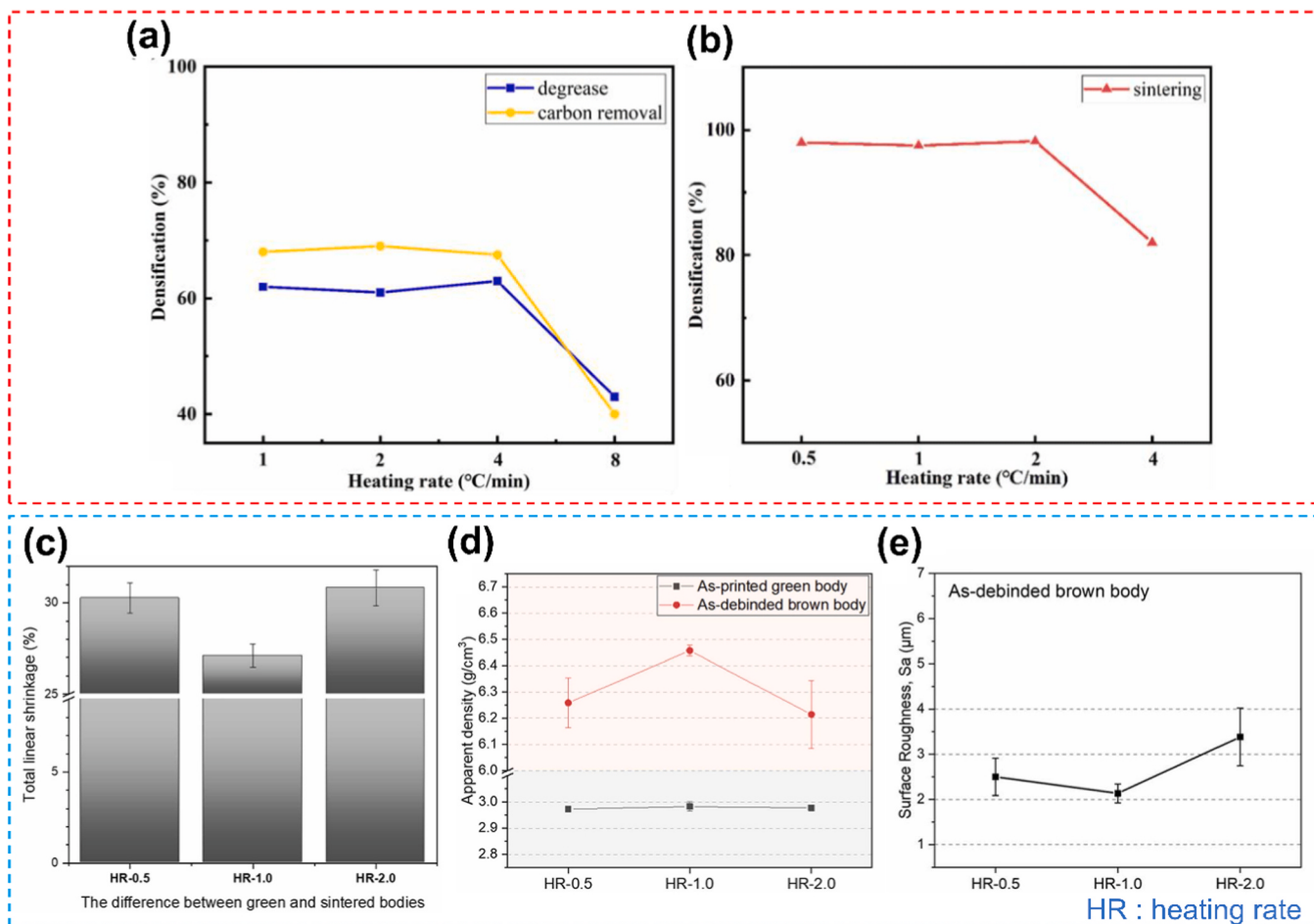


Fig. 26. Effect of the heating rate on different physical properties of the debinded and sintered samples. Densification after (a) debinding, and (b) sintering with different heating rates for BT ceramics fabricated with VP [143]. The variation of the (c) linear shrinkage, (d) density, (e) surface roughness as a function of different heating rates for PZT ceramics fabricated with VP [189].

Reproduced from Ref.: (a-b) [143], Open access article distributed under the terms of the Creative Commons CC BY license, (c-e) [189], with permission from Elsevier.

the decomposition gases generated by the decomposition of the organics at higher temperature.

The debinding cycle shown in Fig. 27(d) has been designed according to the TGA/DTG/DSC plot in Fig. 27(c) and a similar approach to design the debinding schedule has been reported by numerous studies, as evidenced in Table 8 – 10. The binder decomposes in the range of 350 – 550 °C with the intense mass loss happening at around 420 °C (also evidenced by exothermic peak in DSC). The debinding process was carefully designed to gradually increase the temperature in steps, with hold time at certain temperatures (200 °C, 300 °C, 400 °C, 450 °C, 500 °C, and 600 °C for 1 h). This ensures homogeneous heat distribution within the samples, prevents stress development and allows for complete binder decomposition. Subsequently, any residual binder is removed by a second heat treatment in air. In general, this idea of designing the debinding cycle can be applied to samples produced using any other AM technique.

The effect of the binder content on the debinding process can be clearly visualized from Fig. 27(d-e). Samples with a limited amount of organics, such as those fabricated using DIW, can be processed using high heating rates. On the other hand, samples fabricated with VP, usually possess a high amount of binder (~ 18 wt% as shown in Fig. 27(c)) and therefore the debinding rate is slow, making this an energy-intensive process. To increase the energy efficiency of the thermal treatment process, it is necessary to create novel feedstock formulations with low binder content and high ceramic loading.

Similar to VP technique, FFF also requires careful designing of the debinding cycle, because of the high-volume fraction of the binder (typically 40–50 vol%) used in the production of a printable filament. Most of the studies have reported a heating rate in the range of 0.2 – 1 °C/min (Table 9). In a recent study, wick debinding has been successfully used to remove low molecular weight organic wax (paraffin wax) [118]. In this process, the green part is embedded inside a highly porous powder bed which is subsequently heated to a desired temperature. The low molecular weight organic wax begins to melt as the temperature rises and the capillary forces arising from the pores extract the melted wax out of the sample. The final temperature and hold time are important parameters that need to be carefully adjusted. The authors reported that the best results were achieved at isothermal conditions of 200 °C (for 60 h) with a slow heating rate of 0.2 °C/min. Thereafter, the samples could be sintered with a high heating rate of 10 K/min. A recent study reported that the binder decomposition temperature decreases with the increase in the ceramic loadings in the filament [113]. This can be associated with the catalytic effect at the surface of the used ceramic powder [215]. This effect is reported to be more prominent in air when compared to inert atmospheres.

3.2. Sintering and functional properties

In general, after the thermal debinding step, the samples are highly fragile and an additional heat treatment at elevated temperatures below

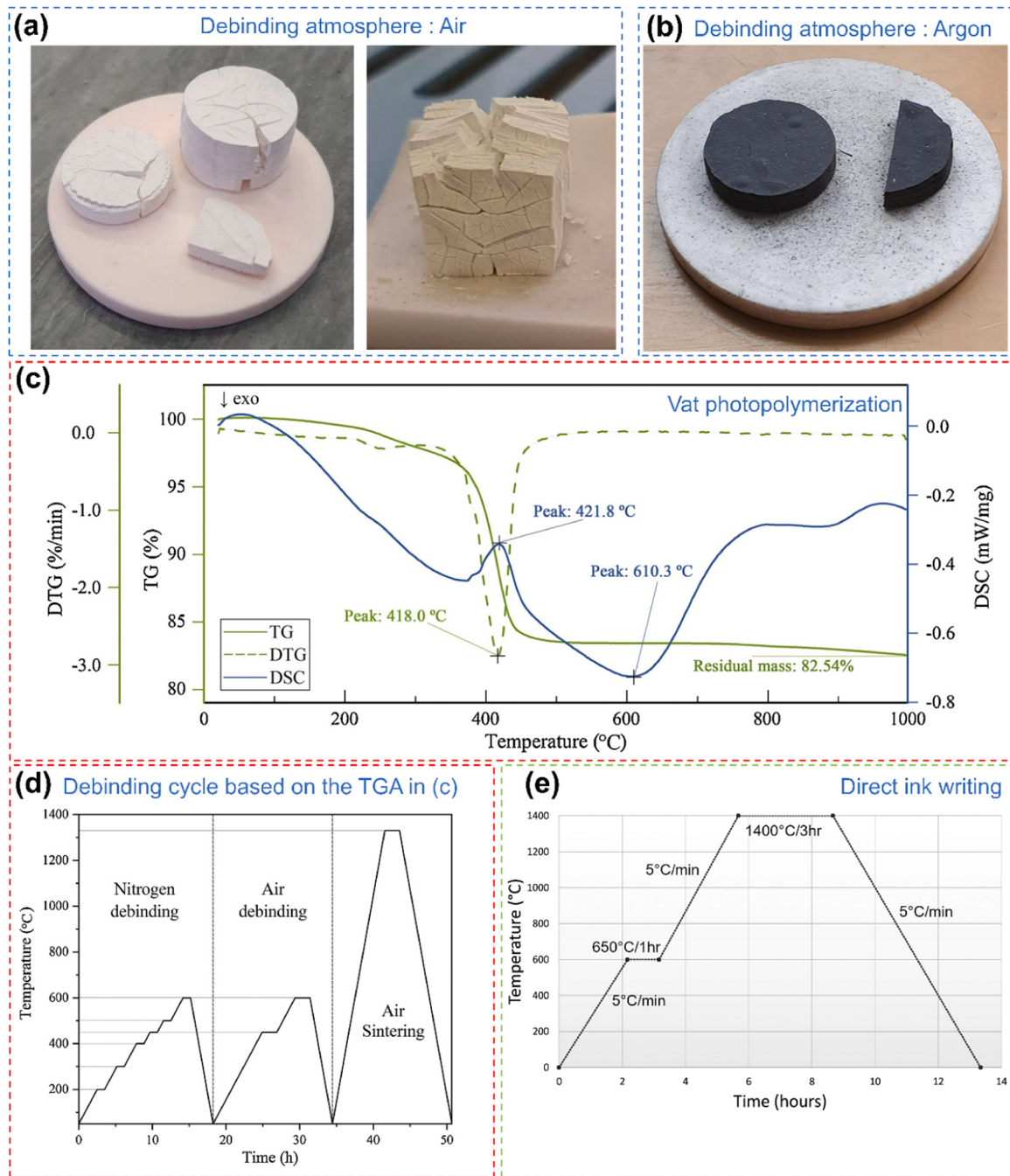


Fig. 27. Comparison of the sample cracking in different atmospheres, accompanied by TGA and corresponding debinding cycles to ensure a defect free sample. (a) Cracks observed in samples during the debinding process in atmospheric air, and (c) Crack free samples when processed in a vacuum, with the black coloration indicating residual carbon content in BT ceramics [159]. (d) TG-DSC analysis of a green body conducted under a nitrogen atmosphere, and (e) the corresponding debinding and sintering process used to sinter the debinded samples [139]. (f) Debinding and sintering profile for samples produced via DIW [86]. Reproduced from Ref.: (a-c) [159], and (d-e) [139], with permission from Elsevier. (f) [86], with permission from John Wiley and Sons.

the melting point (known as sintering) is necessary to achieve high density and desired properties. The desired sintering temperature can be found out by performing a dilatometry test on the powder pressed disc or the printed sample (similar dimension to disc, with flat opposite sides). Kindly note that the dielectric and piezoelectric/ferroelectric measurements are usually carried out on regular-geometry (specially disc shaped samples), as usually required by the equipment.

The most crucial factors that affect the sintering process are the temperature, atmosphere composition, heating rate and the hold time. These variables are crucial in the development of the microstructure, which directly affects the electrical properties, as will be discussed later.

For sintering, alumina crucibles are typically used as a substrate for BT [116] as well as for most of other ceramic materials. The contact area between the sample and the crucible can lead to some unwanted reactions, thus modifying the stoichiometry of the sample. Traces of barium aluminate ($\text{BaO} \bullet \text{Al}_2\text{O}_3$) based compositions are formed in a temperature range between 800 °C and 1400 °C [216]. The sintering of BT takes place at temperatures within this temperature range. To avoid this unwanted reaction with the samples, a platinum wire coil or platinum foil can be used to prevent contact between the sample and the crucible [176]. In the case of compositions containing volatile elements such Pb or K, samples are sintered in a closed alumina crucible using a

powder bed from the same material as the sample to minimise the loss of material and stoichiometry due to volatilization [54,72,74,75,77,83,94,98,104,116,118,121–123,131,133,177].

The relative density of the sintered samples increases with the sintering temperature [73,74,78,86,144]. Further, no further densification occurs by increasing the temperature beyond the temperature where the densification reaches its maximum (also known as over-sintering). In fact, it may even result in a slight decrease in density [51,60,144,149,159,175]. This can be related to the formation of additional porosity due to over-sintering [149]. For instance, Hossain *et al.* reported that, for PZT, a maximum relative density of 97.5 % was achieved at a sintering temperature of 1200 °C. The density decreased slightly on further increasing the sintering temperature to 1300°C (Fig. 28(a)), probably due to loss of volatile PbO in PZT ceramics at such elevated temperatures [74]. This suggests that compositions such as KNN, PMN-PT etc., containing volatile components must be handled with caution during sintering. A similar trend was observed for BCZT. The relative density decreases from 95.88 % to 95.20 % on increasing the temperature to 1525 °C from 1500 °C due to over-sintering (Fig. 28(b)) [149].

Further, the increase in density is also manifested in the form of shrinkage due to decreasing volume of the porosity. In general, owing to the layer by layer build up process, the shrinkage in the z-direction (or, axial) is always higher than the shrinkage in x and y directions (or, radial) [77,144,148–150,152,168,169,172,177,180,183,184,186]. It is

to be noted that the shrinkage (in both directions) decreases when the sample is over-sintered (Fig. 28(c)) [144]. However, surprisingly, some of the studies reported that the converse (shrinkage in x and y higher than in z) is also true [113,139,175,189]. Shrinkage decreases with ceramic loading (Fig. 28(d)) [113,148] and thereafter increases after the optimum loading [139]. An almost similar shrinkage in both directions has also been reported [159].

A recent study reported differences in shrinkage after sintering between dense objects and porous structures, such as TPMS, even though the samples were printed with the same composition [141]. Therefore, to accurately calculate shrinkage in different directions after sintering, it is recommended to print the desired geometry, measure the shrinkage, and then either scale up or scale down according to the desired dimensions.

Along with the density, the grain size also increases with the sintering temperature due to enhanced mass diffusion at elevated temperatures (Fig. 29(a-f)) [73,78,79,83,86,95,113,140,144,184]. In addition to the sintering temperature, dwell or hold times are an important variable affecting the densification process. This can serve various purposes, e.g., an optimized dwell time enhances the particle rearrangement and diffusion rates, thereby ensuring a dense microstructure. Moreover, the dwell time ensures homogeneous temperature distributions, reduces thermal gradients and uneven sintering. In this context, Wei *et al.* studied the effect of different dwell times (2 h, 5 h,

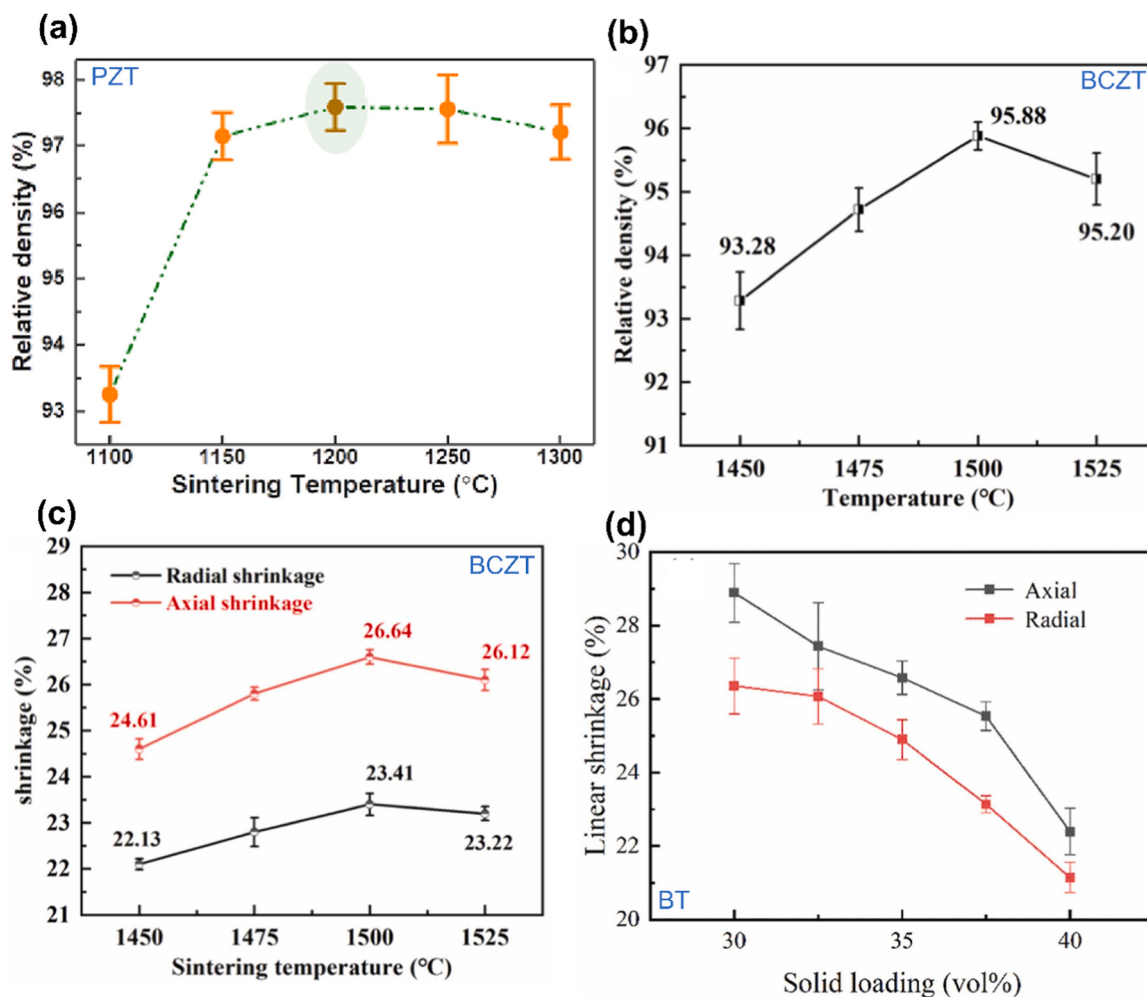


Fig. 28. Effect of sintering temperature and ceramic loadings on the density and shrinkage. (a) Variation in relative density of PZT ceramics as a function of sintering temperature [74]. (b) Linear shrinkage, and (c) Relative density of BCZT ceramics subjected to various sintering temperatures [149]. (d) Linear shrinkage measurements for sintered BT ceramics with varying solid loadings [148].

Reproduced from Ref.: (a) [74], (b-c) [149], and (d) [148], with permission from Elsevier.

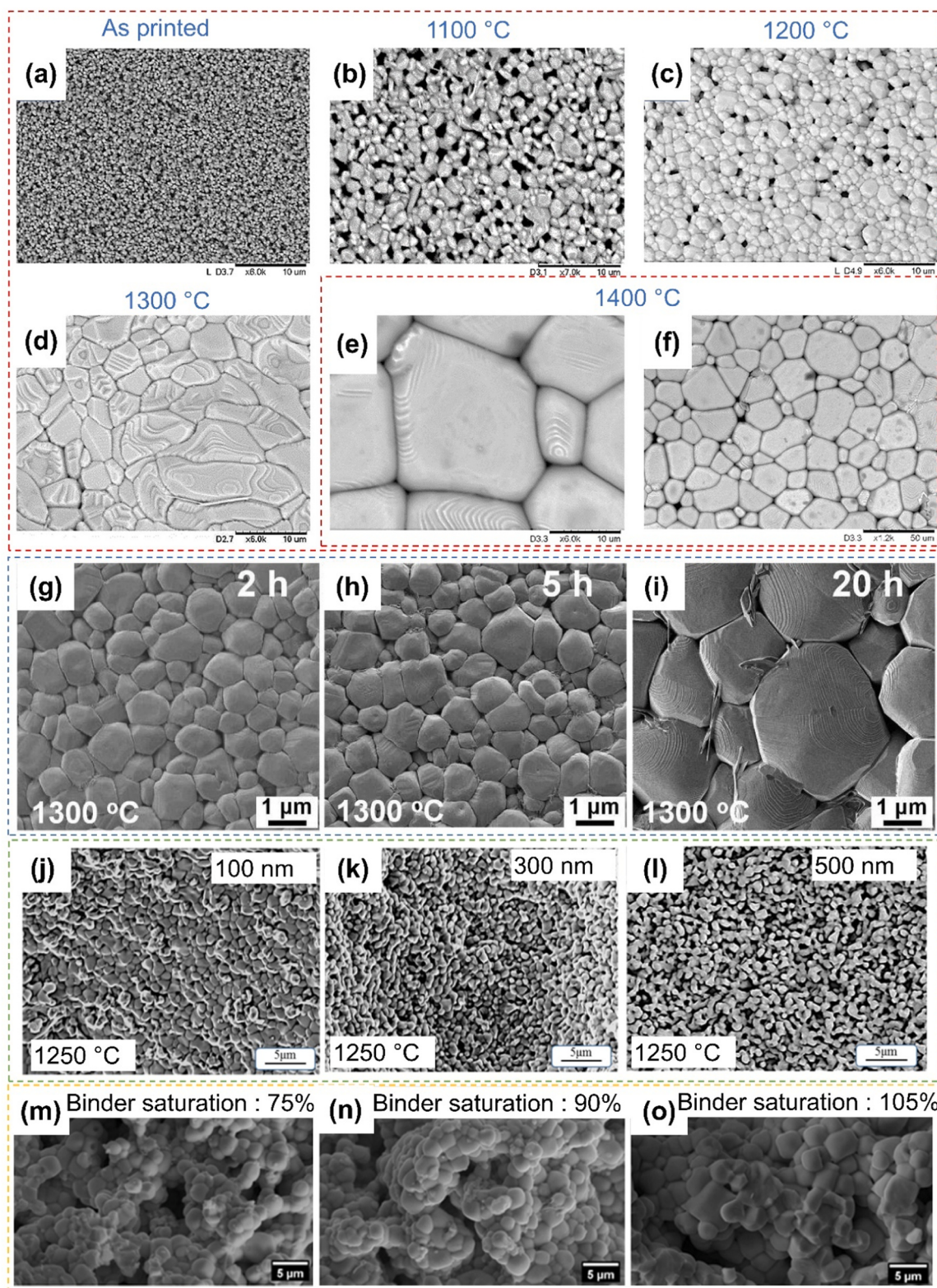


Fig. 29. Various parameters that affect the sintering density and microstructure. SEM images depicting the microstructures of samples at various stages: (a) as printed, and (b-f) sintered at different temperatures [86]. (g-i) SEM micrographs of BT ceramics sintered at 1300°C for different holding times [93]. (j-l) Particle size effect on the microstructure of BT ceramics sintered at same temperature [58]. (m-o) SEM microstructures of binder jetted Nb-doped PZT ceramics sintered at 1250°C with varying binder saturations [199].

Reproduced from Ref.: (a-f) [86], with permission from John Wiley and Sons. (g-i) [93], with permission from Elsevier. (j-l) [58], with permission from IOP Publishing.(m-o) [199], Open access article distributed under the terms of the Creative Commons CC BY license.

and 20 h) at 1300 °C on the densification process and microstructural evolution of BT ceramics [93]. Experimental results pointed out that the relative density increased with the holding time due to the elimination of the pores [183]. However, with prolonged holding time of 20 h, grain growth takes place, with grain sizes reaching almost 2 – 3 µm (Fig. 29(g-i)). The phenomenon of abnormal grain growth observed in BT ceramics is observed after a certain threshold temperature (usually around 1325 °C), where a liquid eutectic phase is formed and thereafter grains may grow abnormally due to Ostwald ripening [113].

The initial particle size is reported to have a profound effect on the densification behaviour of the sintered sample [58]. Often, mechanical milling is employed to break up agglomerates and/or decrease the particle size in the starting feedstock. Finer particles are reported to have better sintering behaviour owing to their large surface area or more increased particle-to-particle contact [147,157]. This has been validated by the findings of Renteria *et al.* [58]. The authors reported that the relative density of the sintered samples increased to almost 85 % from 68 % on changing the initial particle size of 500 nm down to 100 nm. The sample with finer particles exhibited a dense microstructure with slightly bigger grains (due to grain growth) even when sintered under the same conditions. On the contrary, the sample with coarser particles (500 nm) exhibited a significant amount of open porosity with the grain size remaining similar to the initial particle size (Fig. 29(j-l)). This means the thermal activation energy (here, it is the sintering temperature) required to initiate the mass transport phenomenon is higher for coarser particles than for finer particles. Similar results have also been verified for samples fabricated using VP [147].

In contrast to the microstructures shown in Fig. 29(a-f) typically for extrusion-based techniques, the microstructures that are produced by binder-jetted samples are highly porous as depicted in Fig. 29(m-o). Even though the densification increases with the binder saturation value, it still does not reach the levels produced by extrusion or vat photopolymerization. When examining the densification values in Tables 8, 9, 10 and 11, this aspect appears to be clearer.

In general, it is challenging to prepare a feedstock with fine particles. A compromise can be achieved by using particles with a bimodal distribution. In general, inclusion of smaller particles in coarser particles serves to enhance the packing density and consequently the green density of the printed component. In this regard, Renteria *et al.* investigated the effect of bimodal particles (100 and 400 nm) on the packing density and the densification behaviour [61]. The packing density was maximized at 55.8 vol% of large (400 nm) powder particles. It was observed that the densification behaviour is strongly affected by the volume fraction of the fine particles. Surprisingly, the decreasing density was not linear with the increasing coarser fraction. An inflection at 50–50 vol% was observed, suggesting that the final density might be affected by the dominant powder fraction in the sample.

Several studies have demonstrated that density increases with higher solid concentration (as shown in Fig. 30(a)) [148,151,164,169,186]. However, beyond a certain threshold, density may begin to decrease. Possible factors contributing to this include: excessive use of dispersants to lower viscosity [181], limitations in the recoating ability of the scraper blade during printing [139], insufficient curing due to excessive loadings resulting in poor bonding force between layers [151,186], and nozzle clogging leading to uneven flow rates [77]. The addition of low RI materials, generally termed as pore forming agents (PFAs) as discussed in Section 2.3.8, compromises the density to a certain extent after sintering. The porosity increases with increasing amount and size of the PFAs [145,150,152,171,172] and, subsequently, the shrinkage also increases (Fig. 30(b-d)). The inset SEM images in Fig. 30(d) illustrate the difference in microstructure, where an increase in the amount of PFAs results in higher porosity. The quantity of binder utilized in formulating the ink for DIW or in jetting onto the powder bed for BJ also plays a role in determining the final density of the sintered component [85,193]. Deviation from the optimum value led to the formation of large circular pits or residual porosity from the binder burn out. It is worth mentioning

that the sintered microstructure is highly sensitive to the ceramic loadings [181,186]. The grain size increases with the ceramic loading and this can be attributed to the decreasing amount of defects in form of porosity (Fig. 30(e)). Porosity exerts a dragging force to grain boundary motion hindering the grain growth and densification during sintering [217].

It is important to note that the reported density of the samples that are produced using 3D printing is always lower than the density of samples that are powder-pressed [80,113,122,123,146,151,168,179,186]. This is mostly because of the residual porosity generated from the binder-burn out process, as depicted in Fig. 31. Additionally, as observed from Tables 8, 9, 10, and 11, nearly full densification is completely missing in the reported density values. A recent study has further evidenced this fact by carrying out mercury porosimetry analysis on a powder pressed and printed sample. It was found that pore size in the range of 0.1 – 5 µm was attributed to the residual porosity after the binder burn out process as this size fraction of porosity was completely missing in the powder pressed sample [113]. In addition, the presence of printing defects cannot be ignored completely. For samples fabricated using FFF, VP, and DIW, the difference in values between the achieved density and full densification (100 %) is comparatively small (Tables 8, 9, and 10). However, this difference increases significantly for samples fabricated using BJ, where the achieved density is significantly lower (Table 11). This disparity is primarily due to the higher levels of residual porosity mostly generated from the powder-bed packing, which hinders the densification process. Consequently, the piezoelectric performance of the printed components is typically inferior to conventionally powder-pressed samples.

The density of the sintered piezoceramics is strongly affected by the sintering atmosphere as well. In a recent study, authors have utilized innovative sintering processes such as ultra-fast high temperature sintering (UHS), pressure-less spark plasma sintering (P-SPS) and fast firing (FF) to achieve rapid debinding and sintering of the BT components fabricated using DIW [79]. The experiments were carried out in inert atmosphere for UHS (Ar/N₂) and P-SPS (Ar) to prevent the oxidation of the graphite felt or the die at such high temperatures. On the other hand, fast firing experiments were conducted in ambient conditions. The samples were able to resist the rapid heating and cooling rates, without any noticeable defects in the samples. However, the densification was restricted to around 70 – 78 % for samples sintered using UHS and P-SPS (Fig. 32(a-b)). On the contrary, samples sintered using FF exhibited high densities of up to 95 % (Fig. 32(b)). The authors reported that the phase transition from tetragonal to hexagonal, while sintering in inert atmospheres (Fig. 32(c-e)), adversely affects densification by enhancing the pore-grain boundary separation and anisotropic coarsening (formation of elongated grains) as shown in Fig. 32(h-i, k-l, n-o). Such elongated grains are typical for the hexagonal phase. Additionally, the samples exhibited dark coloration which was correlated to the reduction of the oxide in such low p(O₂) conditions. Similar observation was made for BT ceramics sintered using SLS [205]. In contrast, when sintered in air, the tetragonal phase was retained with dense microstructure and equiaxed grains (Fig. 32(f, p-r)). The tetragonal phase was also retained at lower UHS currents (20 A) and P-SPS temperature (1300 °C), however no densification was observed as the thermal activation energy for mass diffusion was insufficient as evidenced in Fig. 32(g, j, m).

A similar phase transformation has been reported for samples sintered using SLS [205,207]. Such phase transition is reported to occur at 1460 °C in air. However, when sintering in H₂ atmosphere, the phase transition temperature decreases to 1360 °C which can be related to the formation of oxygen vacancies and Ti³⁺ which stabilizes the high temperature hexagonal phase at room temperature [218,219]. In addition, the very high cooling rates achieved in SLS (similar to UHS) can be one of the most probable mechanisms that helps in retaining the meta-stable phase at room temperature [206,207,210]. The high cooling rates achieved during such process helps in retaining a fine very microstructure, which otherwise would have been difficult to achieve [210]. Similar to

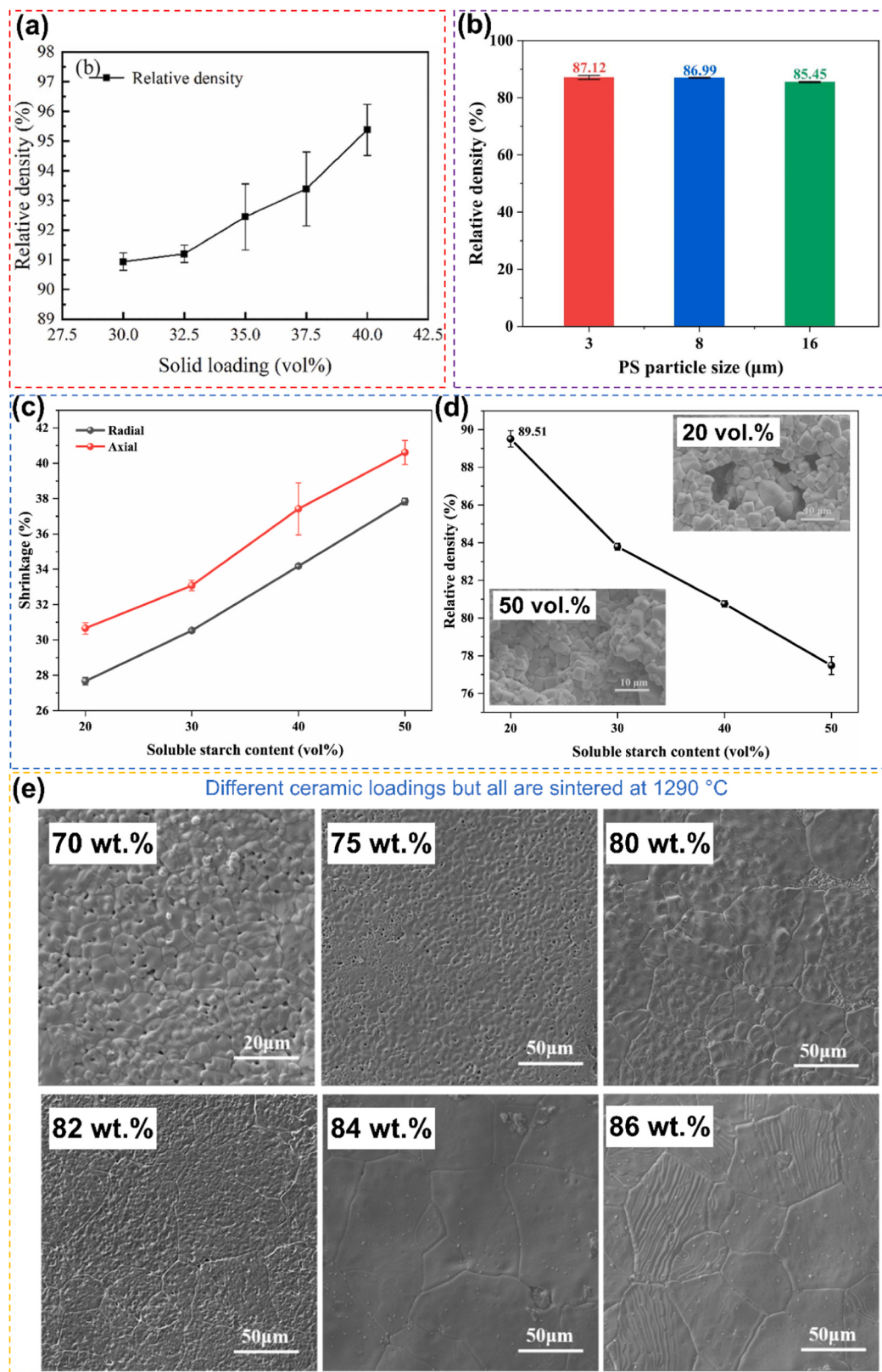


Fig. 30. Effect of the ceramic loadings and PFAs on the density, shrinkage and microstructure of the sintered ceramic. (a) Relative density measurements of sintered BT ceramics with varying solid loadings [148]. (b) Relative density as a function of different PS particle sizes [152]. (c) Shrinkage, and (d) Relative density of PZT piezoceramics as a function of different amount of soluble starch content. The insert in (d) shows the SEM images after sintering with different amount of SS [150]. (e) SEM micrographs as a function of different ceramic loadings sintered at same temperature [181].

Reproduced from Ref.: (a) [148], (b) [152], and (c-d) [150], with permission from Elsevier. (e) [181], Open access article distributed under the terms of the Creative Commons CC BY license.

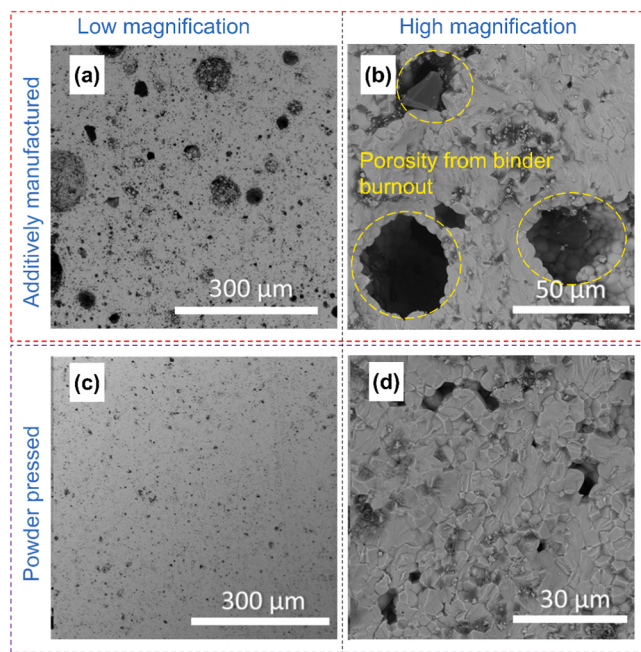


Fig. 31. SEM micrographs of sintered PZT ceramics exhibiting the difference between the (a-b) 3D printed sample and (c-d) a powder pressed sample [77]. Reproduced from Ref.: (a-d) [77], with permission from Elsevier.

the UHS process, the temperature control during the SLS process is very challenging. Usually, the laser spot follows a Gaussian distribution of energy with the maximum being achieved at the centre of the spot [205]. Thus, it is quite challenging to maintain the same temperature at each scanning spot on the powder bed, which then leads to inhomogeneity.

Since most of these piezoelectric materials have a crystalline structure, XRD is the most widely used method to study the structure and phases. As an alternative, Raman analysis is sometimes carried out for determining the developed phases as well [113,151,186].

With XRD, the lattice parameters are accessible and a unit cell distortion can be calculated. The unit cell distortion describes the distortion from the paraelectric cubic phase. The spontaneous polarisation in ferroelectric phases is oriented along the direction of the unit cell distortion, which is the $[001]_{pc}$ direction in tetragonal symmetry, the $[110]_{pc}$ direction in orthorhombic symmetry, the $[111]_{pc}$ direction in rhombohedral symmetry or more complex directions in monoclinic symmetry [220]. The subscript “pc” refers to the pseudocubic undistorted perovskite unit cell. The unit cell distortion increases with increasing lattice parameters towards the direction of the spontaneous polarisation [113,147]. The intrinsic piezoelectric effect has a direct proportional relationship to the unit cell distortion. In ferroelectric ceramics with tetragonal symmetry, the unit cell distortion is referred to as tetragonality and is defined as the c/a ratio, which is the ratio of the long c-axis (c) to the short a-axis (a) of the crystal structure.

The tetragonality is reported to increase with the sintering temperature as depicted in Fig. 33(a) [86,113,149]. This increase is evidenced by the enhanced 200 reflection splitting to 200_T and 002_T in XRD patterns, indicating a greater degree of unit cell distortion after the phase transformation from cubic to tetragonal symmetry, i.e., for Cu K α radiation these reflections are located around of $2\theta = 45^\circ$. This is also evidenced by high c/a ratio (also denoted by η_T) for the sample sintered at 1350°C with bigger grains ($> 20 \mu\text{m}$) (Fig. 33(b)).

The initial particle size also affects the tetragonality of ferroelectric ceramics. Fine powders require less energy and hence are expected to exhibit higher tetragonality when compared to coarse powders processed in the same conditions [58,59,61,158]. This can be related to the final grain size of the sintered ceramic. For instance, Reneteria *et al.*

reported that the samples fabricated with 100 nm particles exhibited a grain size of approximately $1.18 \mu\text{m}$ after sintering [58]. On the other hand, the 300 nm and 500 nm particles exhibited a grain size of approximately 871 nm and 757 nm, respectively. It should be noted that the sintering temperature was similar for all particle sizes. However, the sample processed from 100 nm particles showed the highest 200 reflection splitting. In an another study, authors have used different sintering temperatures for different particles sizes; 1300°C for 200 nm and 1330°C for 600 nm particles sizes [147]. The sample processed from 600 nm particle sizes and a final grain size of 875 nm exhibited higher reflection splitting (Fig. 33(c)). It is widely accepted that the tetragonality decreases on reducing the grain size of the sintered ceramic. This is due to increased internal stresses generated by the high volume of grain boundaries and domain walls [15,16,221]. Smaller grains have a higher domain wall density, leading to higher internal stresses that hinder the crystal lattice distortion, lowering the c/a ratio. In contrast, larger grains, with lower domain wall density and lower stresses, maintain higher tetragonality (high c/a ratio). Since a higher ceramic loading results in a microstructure with less porosity and larger grains, it will also result in a higher tetragonality [164,181].

Polycrystalline ceramics are considered to consist of a microstructure of randomly oriented grains. However, if there is a preferential orientation, it can be detected and quantified by XRD analysis. This anisotropy of the distribution of crystallographic directions is called texture. XRD patterns are used to evaluate or understand the degree of texturing. For instance, Lorenz *et al.* investigated the diffraction patterns of sintered BT, measured parallel and perpendicular with respect to the extrusion direction in reflection geometry at the surface (Fig. 33(d)) [70]. The authors reported that the variation in the reflection intensities along different directions is due to the preferential particle alignment along the extrusion direction during the printing process. In general, the Lotgering factor (F) is often used to quantify the degree of texturing [91, 102,162,163] and it can be calculated using Eq. 15 [222]:

$$F = \frac{(I - I_0)}{(1 - I_0)} \quad (15)$$

where, I_0 is the reflection intensity of a sample with random orientation and I the reflection intensity of a textured sample. The Lotgering factor is calculated with the intensities of characteristic reflections for the respective symmetry. Walton *et al.* reported that the Lotgering factor F declines on advancing from the surface ($F \sim 40$) of a filament to ($F \sim 0$) at the centre of a filament, as also depicted in the microstructure in (Fig. 9(c)) [91]. This is in accordance with the torque simulation findings carried out on the filaments. Highest torque is experienced on the surface, while least in the core. A low Lotgering factor of 0.46 was reported in case of additively manufactured bismuth titanate [102]. The authors reported that the initial matrix particles were quite coarse ($0.5 - 1 \mu\text{m}$), which led to a sluggish grain growth. Another probable reason could be the lack of alignment of the templates during the extrusion process itself. In a recent study, the authors have shown that the degree of texturing increases (from 94.3 % to 97.4 %) with sintering temperature (increasing from 1250°C to 1300°C) due to templated grain growth of the used seed platelets (Fig. 33(e)) [163]. However, as the temperature increases above a certain temperature, grain growth of the matrix grains occurs without any distinct texture, resulting in an overall reduced texturing.

Often, researchers use sintering aids to lower the sintering temperature by forming a liquid phase. The mass transport and diffusion phenomena are reported to be higher in the presence of a liquid phase due to increased atomic mobility compared to solid-state sintering. In addition, the residual porosity left after binder burn out often limits the degree of texturing as well. Copper oxide (CuO) is one of the most widely used sintering aids reported in the literature [163,184]. He *et al.* reported that the density and the grain size increased with increasing CuO content up to 1.5 mol.% (Fig. 34(b-c)) [184]. Excess CuO (2 mol.%) resulted in a